

# Single-fluorophore orientation determination with multiview polarized illumination: modeling and microscope design

TALON CHANDLER,<sup>1,\*</sup> SHALIN MEHTA,<sup>1,2,3</sup> HARI SHROFF,<sup>4,5</sup>  
RUDOLF OLDENBOURG,<sup>2,6</sup> AND PATRICK J. LA RIVIÈRE<sup>1,5</sup>

<sup>1</sup>*University of Chicago, Department of Radiology, Chicago, Illinois 60637, USA*

<sup>2</sup>*Marine Biological Laboratory, Bell Center, Woods Hole, Massachusetts 02543, USA*

<sup>3</sup>*(present address) Chan Zuckerberg Biohub, San Francisco, California 94158, USA*

<sup>4</sup>*Section on High Resolution Optical Imaging, National Institute of Biomedical Imaging and Bioengineering, National Institutes of Health, Bethesda, Maryland 20892, USA*

<sup>5</sup>*Marine Biological Laboratory, Whitman Center, Woods Hole, Massachusetts 02543, USA*

<sup>6</sup>*Brown University, Department of Physics, Providence, Rhode Island 02912, USA*

\*[talonchandler@talonchandler.com](mailto:talonchandler@talonchandler.com)

**Abstract:** We investigate the use of polarized illumination in multiview microscopes for determining the orientation of single-molecule fluorescence transition dipoles. First, we relate the orientation of single dipoles to measurable intensities in multiview microscopes and develop an information-theoretic metric—the solid-angle uncertainty—to compare the ability of multiview microscopes to estimate the orientation of single dipoles. Next, we compare a broad class of microscopes using this metric—single- and dual-view microscopes with varying illumination polarization, illumination numerical aperture (NA), detection NA, obliquity, asymmetry, and exposure. We find that multi-view microscopes can measure all dipole orientations, while the orientations measurable with single-view microscopes is halved because of symmetries in the detection process. We also find that choosing a small illumination NA and a large detection NA are good design choices, that multiview microscopes can benefit from oblique illumination and detection, and that asymmetric NA microscopes can benefit from exposure asymmetry.

© 2017 Optical Society of America

**OCIS codes:** (110.0110) Imaging systems; (180.2520) Fluorescence microscopy; (180.0180) Microscopy; (180.6900) Three-dimensional microscopy; (130.5440) Polarization-selective devices; (260.5430) Polarization.

## References and links

1. E. J. Peterman, H. Sosa, L. S. Goldstein, and W. E. Moerner, “Polarized fluorescence microscopy of individual and many kinesin motors bound to axonemal microtubules,” *Biophys. J.* **81**, 2851–2863 (2001).
2. J. N. Forkey, M. E. Quinlan, M. A. Shaw, J. E. T. Corrie, and Y. E. Goldman, “Three-dimensional structural dynamics of myosin V by single-molecule fluorescence polarization,” *Nature* **422**, 399–404 (2003).
3. A. S. Backer, M. Lee, and W. E. Moerner, “Enhanced DNA imaging using super-resolution microscopy and simultaneous single-molecule orientation measurements,” in “Conference on Lasers and Electro-Optics,” (Optical Society of America, 2016), p. JTh4B.4.
4. S. B. Mehta, M. McQuilken, P. J. La Rivière, P. Occhipinti, A. Verma, R. Oldenbourg, A. S. Gladfelter, and T. Tani, “Dissection of molecular assembly dynamics by tracking orientation and position of single molecules in live cells,” *Proc. Natl. Acad. Sci. U.S.A.* **113**, E6352–E6361 (2016).
5. B. DeMay, N. Noda, A. Gladfelter, and R. Oldenbourg, “Rapid and quantitative imaging of excitation polarized fluorescence reveals ordered septin dynamics in live yeast,” *Biophys. J.* **101**, 985–994 (2011).
6. M. McQuilken, M. S. Jentzsch, A. Verma, S. B. Mehta, R. Oldenbourg, and A. S. Gladfelter, “Analysis of septin reorganization at cytokinesis using polarized fluorescence microscopy,” *Front. Cell Dev. Biol.* **5**, 42 (2017).
7. A. Anantharam, B. Onoa, R. H. Edwards, R. W. Holz, and D. Axelrod, “Localized topological changes of the plasma membrane upon exocytosis visualized by polarized TIRFM,” *J. Cell Biol.* **188**, 415–428 (2010).
8. M. P. Backlund, M. D. Lew, A. S. Backer, S. J. Sahl, and W. E. Moerner, “The role of molecular dipole orientation in single-molecule fluorescence microscopy and implications for super-resolution imaging,” *ChemPhysChem* **15**, 587–599 (2014).
9. M. A. Lieb, J. M. Zavislan, and L. Novotny, “Single-molecule orientations determined by direct emission pattern imaging,” *J. Opt. Soc. Am. B* **21**, 1210–1215 (2004).

10. A. S. Backer and W. E. Moerner, “Extending single-molecule microscopy using optical Fourier processing,” *J. Phys. Chem. B* **118**, 8313–8329 (2014).
11. A. Agrawal, S. Quirin, G. Grover, and R. Piestun, “Limits of 3D dipole localization and orientation estimation for single-molecule imaging: towards Green’s tensor engineering,” *Opt. Express* **20**, 26667–26680 (2012).
12. E. Toprak, J. Enderlein, S. Syed, S. A. McKinney, R. G. Petschek, T. Ha, Y. E. Goldman, and P. R. Selvin, “Defocused orientation and position imaging (DOPI) of myosin V,” *Proc. Natl. Acad. Sci. U.S.A.* **103**, 6495–6499 (2006).
13. A. Débarre, R. Jaffiol, C. Julien, D. Nutarelli, A. Richard, P. Tchénio, F. Chaput, and J.-P. Boilot, “Quantitative determination of the 3D dipole orientation of single molecules,” *Eur. Phys. J. D.* **28**, 67–77 (2004).
14. M. Shribak and R. Oldenbourg, “Techniques for fast and sensitive measurements of two-dimensional birefringence distributions,” *Appl. Opt.* **42**, 3009–3017 (2003).
15. J. T. Fourkas, “Rapid determination of the three-dimensional orientation of single molecules,” *Opt. Lett.* **26**, 211–213 (2001).
16. J. S. Tyo, D. L. Goldstein, D. B. Chenuant, and J. A. Shaw, “Review of passive imaging polarimetry for remote sensing applications,” *Appl. Opt.* **45**, 5453–5469 (2006).
17. C.-Y. Lu and D. A. Vanden Bout, “Analysis of orientational dynamics of single fluorophore trajectories from three-angle polarization experiments,” *J. Chem. Phys.* **128**, 244501 (2008).
18. Y. Wu, P. Wawrzusin, J. Senseney, R. S. Fischer, R. Christensen, A. Santella, A. G. York, P. W. Winter, C. M. Waterman, Z. Bao, D. A. Colon-Ramos, M. McAuliffe, and H. Shroff, “Spatially isotropic four-dimensional imaging with dual-view plane illumination microscopy,” *Nat. Biotechnol.* **31**, 1032–1038 (2013).
19. R. K. Chhetri, F. Amat, Y. Wan, B. Hockendorf, W. C. Lemon, and P. J. Keller, “Whole-animal functional and developmental imaging with isotropic spatial resolution,” *Nat. Methods* **12**, 1171–1178 (2015).
20. Y. Wu, P. Chandris, P. W. Winter, E. Y. Kim, V. Jaumouillé, A. Kumar, M. Guo, J. M. Leung, C. Smith, I. Rey-Suarez, H. Liu, C. M. Waterman, K. S. Ramamurthi, P. J. La Rivière, and H. Shroff, “Simultaneous multiview capture and fusion improves spatial resolution in wide-field and light-sheet microscopy,” *Optica* **3**, 897–910 (2016).
21. Y. Wu, A. Kumar, C. Smith, E. Ardiel, P. Chandris, R. Christensen, I. Rey-Suarez, M. Guo, H. Vishwasrao, J. Chen, J. Tang, A. Upadhyaya, P. La Rivière, and H. Shroff, “Reflective imaging improves resolution, speed, and collection efficiency in light sheet microscopy,” *bioRxiv* (2017).
22. S. M. Kay, *Fundamentals of statistical signal processing* (Prentice Hall PTR, 1993).
23. T. W. Anderson, *An introduction to multivariate statistical analysis* (Wiley, 1958).
24. D. Coe, “Fisher matrices and confidence ellipses: a quick-start guide and software,” arXiv preprint arXiv:0906.4123 (2009).
25. S. van der Walt, S. C. Colbert, and G. Varoquaux, “The NumPy array: a structure for efficient numerical computation,” *CoRR* **abs/1102.1523** (2011).
26. A. Meurer, C. P. Smith, M. Paprocki, O. Čertík, S. B. Kirpichev, M. Rocklin, A. Kumar, S. Ivanov, J. K. Moore, S. Singh, T. Rathnayake, S. Vig, B. E. Granger, R. P. Muller, F. Bonazzi, H. Gupta, S. Vats, F. Johansson, F. Pedregosa, M. J. Curry, A. R. Terrel, v. Roučka, A. Saboo, I. Fernando, S. Kulal, R. Cimrman, and A. Scopatz, “SymPy: symbolic computing in Python,” *PeerJ Computer Science* **3**, e103 (2017).
27. J. D. Hunter, “Matplotlib: A 2D graphics environment,” *Computing In Science & Engineering* **9**, 90–95 (2007).
28. L. Campagnola, A. Klein, E. Larson, A. Griffiths, C. Rossant, N. P. Rougier, I. Zaid, M. S. Suraj, A. Taylor, sylm21, M. F. Kaptan, A. J. Champandard, karlcz, nippoo, Siddharth, X. Gao, C. GESTES, bdurin, J. D. Reaver, R. McMullen, FiachAntaw, T. Mansencal, M. Dartailh, StephenWest, J. Kieffer, G. Baty, R. Peters, macduff111, E. S. de Andrade, and D. Rufat, “vispy: Version 0.4.0,” (2015).
29. J. C. Bowman and A. Hammerlindl, “Asymptote: A vector graphics language,” *TUGBOAT* **29**, 288–294 (2008).
30. L. Novotny and B. Hecht, *Principles of Nano-Optics* (Cambridge University, 2006).
31. M. Levoy, R. Ng, A. Adams, M. Footer, and M. Horowitz, “Light field microscopy,” in “ACM SIGGRAPH 2006 Papers,” (ACM, New York, NY, USA, 2006), SIGGRAPH ’06, pp. 924–934.

---

## 1. Introduction

The orientation of single-molecule fluorescence transition dipoles is a valuable reporter for biological processes. By imaging biological samples with fluorescent probes that are fixed to known structures, researchers have studied the dynamics of motor proteins [1, 2], DNA [3], actin [4], septin [5, 6], and membranes [7]. The number of techniques available to biologists for measuring the orientation of single dipoles in live cells is continually expanding. A recent review [8] identified three major categories of single-dipole orientation determination techniques:

**Spatial/angular variation of emission** techniques image single molecules and use the distribution of intensity in the back focal plane [9] or in the image plane [10] to estimate their dipole orientation. Information-theoretically optimal techniques in this category use defocusing or phase masks in the back focal plane to encode orientation and position information in the image [11]. These techniques can estimate the orientation of dipoles in all orientations and

only require a single frame of intensity measurements, but they require complex reconstruction algorithms, expensive high numerical aperture (NA) optics, and sensitive detectors. Furthermore, these techniques spread the signal from a single molecule over a large area on the detector, so they suffer from a poor signal-to-noise ratio [12].

**Spatial variation of illumination polarization** techniques vary the polarization and intensity in the illumination path to excite dipoles in specific orientations in the focal volume [13]. Although these techniques can accurately estimate the orientation of dipoles in all orientations, they require scanning which makes acquisition time a concern in live-cell imaging.

**Polarized illumination or detection** techniques vary the polarization of light in the illumination or detection paths and exploit the anisotropic absorption and emission patterns of single molecules to estimate their dipole orientation. By illuminating and detecting from the focal plane, not just the focal point, these techniques can estimate the orientation of many dipoles in parallel without scanning. These techniques are easy to implement—changing the illumination or detection polarization is simple with a polarization splitter [4] or universal compensator/polarizer [14]—and the reconstruction methods are straightforward [3, 4, 15]. Also, these techniques keep the signal from a single molecule localized on the detector, so they have a signal-to-noise ratio advantage over defocusing and phase masking techniques. The main drawback is that these techniques require several intensity measurements under different polarization orientations to estimate the orientation of a single dipole. Despite the requirement for multiple measurements, polarized illumination or detection methods are good choices for live-cell imaging because of their combination of speed and ease of implementation.

To develop a polarized illumination or detection technique we need to choose a method for varying the polarization and place it in the illumination or detection path. The simplest and most inexpensive way to vary the polarization is with a division-of-time (DoT) polarizer using a rotating polarizer or a universal compensator/polarizer. Other polarization methods (division-of-amplitude, division-of-focal-plane) are more expensive and require additional alignment or interpolation [16]. The simplicity of DoT polarization comes at the expense of temporal resolution—intensity measurements are made one after the other which increases the acquisition time. If we place the DoT polarizer in the detection path, we will block valuable photons from reaching the detector which leads to unnecessary exposure to the sample [5]. By placing the DoT polarizer in the illumination arm we minimize exposure to the sample. We focus on DoT polarized illumination in this paper because of its combination of simplicity and low sample exposure.

All single-dipole orientation determination methods suffer from some degree of anisotropic orientation uncertainty, i.e., some dipole orientations cannot be determined as precisely as others. In some cases the orientation cannot be determined at all—the forward model can be degenerate for specific dipole orientations [15, 17]. We feel that the importance of isotropic orientation uncertainty has been underappreciated. To our knowledge, the only authors who have considered anisotropic orientation uncertainty in 3D have only analyzed a subset of dipole orientations [11]. Our view is that an ideal technique for determining the orientation of single dipoles can reconstruct the orientation with a small and nearly uniform uncertainty for all dipole orientations.

Recently, there has been increasing interest in multiview microscopy techniques for biological imaging [18–21]. Multiview microscopes offer two major advantages over single-view microscopes. First, multiview microscopes can achieve nearly isotropic resolution compared to the anisotropic resolution of single-view microscopes whose axial resolution is reduced by at least a factor of two compared to lateral resolution. Second, multiview microscopes can use light-sheet illumination to reduce phototoxicity while reusing parts of the optical path for both illumination and detection. For example, if two orthogonal objectives are focused on the same point, then the objectives can alternate roles as the light-sheet illumination path and as the detection path.

Light-sheet illumination offers a major reduction of phototoxicity because a light sheet only illuminates in-focus regions while other widefield and confocal approaches inevitably illuminate out-of-focus regions. Together, these advantages make multiview microscopes good candidates for imaging live biological specimens for long periods.

In this work we explore the use of polarized illumination in multiview microscopes for determining the orientation of single dipoles. Existing multiview microscopes can easily be outfitted with fast-switching polarizers that do not degrade image quality, so polarized illumination is a natural way to augment multiview microscopes for measuring the orientation of single dipoles. Furthermore, multiview microscopes can achieve nearly isotropic resolution while delivering selective illumination. We find that multiview microscopes also provide a small and uniform orientation uncertainty for single dipoles in all orientations. We also find that single-view microscopes have symmetries that can be broken by adding a second view. This reduction of degeneracy allows multiview microscopes to uniquely determine the orientation of single dipoles.

In section 2 we develop the theory required to model polarized illumination microscopes, and we develop metrics to compare microscope designs. In section 3 we compare the results for a wide range of multiview microscope designs. Finally, in section 4 we discuss the results and their impact on polarized multiview microscope design.

## 2. Methods

In this section we develop a method to compare multiview polarized illumination microscopes for the task of reconstructing dipole orientations. In sections 2.1–2.4 we develop a model for the intensity collected with a fixed illumination and detection configuration as a function of the dipole orientation. In section 2.5 we list a variety of ways to combine these intensity measurements into experimentally realizable polarized illumination microscopes. Finally, in section 2.6 we develop metrics that we will use to compare these microscopes.

We use roman type for scalars, e.g.,  $\phi, \theta$ ; bold lowercase type for vectors, e.g.,  $\mathbf{r}, \boldsymbol{\mu}$ ; hats for unit vectors, e.g.,  $\hat{\mathbf{r}}, \hat{\boldsymbol{\mu}}$ ; and bold capital type for matrices, e.g.,  $\mathbf{R}, \mathbf{F}$ .

### 2.1. Absorption Efficiency

In this section we will calculate the *absorption efficiency* of a single dipole—the fraction of the incident power that is absorbed by the dipole. Our approach is inspired by Fourkas [15], but here we calculate the absorption efficiency instead of the detection efficiency.

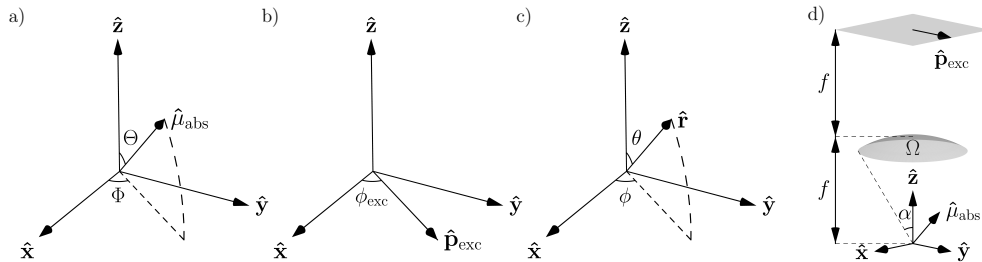


Fig. 1. Coordinate systems for a) the absorption dipole moment  $\hat{\boldsymbol{\mu}}_{\text{abs}}$ , b) the polarizer transmission axis  $\hat{\mathbf{p}}_{\text{exc}}$ , and c) the dummy integration vector  $\hat{\mathbf{r}}$ . d) The scene consists of a single molecule at the focal point of an objective lens with a polarizer in the aperture plane.

We consider a single molecule with a fixed absorption dipole moment  $\hat{\boldsymbol{\mu}}_{\text{abs}}$  that we express in

spherical coordinates  $\Theta$  and  $\Phi$  [see Fig. 1(a)] as

$$\hat{\mu}_{\text{abs}}(\Theta, \Phi) = \sin \Theta \cos \Phi \hat{x} + \sin \Theta \sin \Phi \hat{y} + \cos \Theta \hat{z}. \quad (1)$$

We place the molecule in the focal plane of an ideal, aplanatic, polarization-preserving objective lens with its optical axis aligned with the  $\hat{z}$  axis. Next, we place a polarizer in the aperture plane with a variable transmission axis  $\hat{p}_{\text{exc}}$  that we express as

$$\hat{p}_{\text{exc}}(\phi_{\text{exc}}) = \cos \phi_{\text{exc}} \hat{x} + \sin \phi_{\text{exc}} \hat{y}, \quad (2)$$

where  $\phi_{\text{exc}}$  is the angle between the transmission axis of the polarizer and the positive  $\hat{x}$  axis [see Fig. 1(b)]. Finally, we place a spatially incoherent and spatially uniform light source (or its image) in the aperture plane to illuminate the focal plane. In this geometry each point in the sample is illuminated by a range of angles that can be changed by adjusting the radius of the diaphragm in the aperture plane. We denote the set of illuminated angles by  $\Omega$  [see Fig. 1(d)]. If we use unit vectors  $\hat{r}$  expressed in spherical coordinates  $\theta$  and  $\phi$  [see Fig. 1(c)] as

$$\hat{r}(\theta, \phi) = \sin \theta \cos \phi \hat{x} + \sin \theta \sin \phi \hat{y} + \cos \theta \hat{z}, \quad (3)$$

then the set of angles  $\Omega$  can be expressed as

$$\Omega = \{\phi, \theta \mid 0 < \phi \leq 2\pi, 0 < \theta \leq \alpha\}, \quad (4)$$

where  $\alpha$  is the angle between the optical axis and the most oblique illuminating ray. Equivalently,  $\alpha$  can be expressed in terms of NA using

$$\text{NA} = n \sin \alpha, \quad (5)$$

where  $n$  is the index of refraction of the sample medium. Note that the NA of the objective is always greater than or equal to the illumination NA because we can underfill the aperture plane.

The objective focuses the light by applying a position-dependent rotation to the electric field which we model by multiplying the incident electric field  $\hat{p}_{\text{exc}}$  by a position-dependent rotation matrix

$$\mathbf{R}(\hat{r}) = \begin{bmatrix} \cos \theta \cos^2 \phi + \sin^2 \phi & (\cos \theta - 1) \sin \phi \cos \phi & \sin \theta \cos \phi \\ (\cos \theta - 1) \sin \phi \cos \phi & \cos \theta \sin^2 \phi + \cos^2 \phi & \sin \theta \sin \phi \\ -\sin \theta \cos \phi & -\sin \theta \sin \phi & \cos \theta \end{bmatrix}. \quad (6)$$

Note the difference of signs between Eq. (6) and the rotation matrix given by Fourkas—our matrix rotates rays propagating towards the sample while Fourkas' matrix rotates rays propagating away from the sample.

To find the absorption efficiency  $\eta_{\text{abs}}$  of a single dipole if it were illuminated by a single ray, we take the unit incident electric field  $\hat{p}_{\text{exc}}$ , take the dot product with the absorption dipole moment, then take the modulus squared

$$\eta_{\text{abs}}^{\text{ray}} = |\hat{\mu}_{\text{abs}} \cdot \hat{p}_{\text{exc}}|^2. \quad (7)$$

To find the absorption efficiency of a single dipole, we integrate over all illumination rays and divide by the total incident power which gives the vector expression

$$\eta_{\text{abs}} = \frac{\int_{\Omega} d\hat{r} |\hat{\mu}_{\text{abs}} \cdot \mathbf{R}(\hat{r}) \hat{p}_{\text{exc}}|^2}{\int_{\Omega} d\hat{r}}. \quad (8)$$

We substitute Eqs. (1)–(6) into Eq. (8), evaluate the integrals, and simplify to express the absorption efficiency in scalar notation as

$$\eta_{\text{abs}} = D \{ A + B \sin^2 \Theta + C \sin^2 \Theta \cos [2(\Phi - \phi_{\text{exc}})] \} \quad (9)$$

where

$$A = \frac{1}{4} - \frac{3}{8} \cos \alpha + \frac{1}{8} \cos^3 \alpha \quad (10a)$$

$$B = \frac{3}{16} \cos \alpha - \frac{3}{16} \cos^3 \alpha \quad (10b)$$

$$C = \frac{7}{32} - \frac{3}{32} \cos \alpha - \frac{3}{32} \cos^2 \alpha - \frac{1}{32} \cos^3 \alpha \quad (10c)$$

$$D = \frac{4}{3(1 - \cos \alpha)}. \quad (10d)$$

Note that the factor  $D$  keeps the specimen irradiance constant for any value of  $\alpha$ . We have kept  $D$  as a multiplicative factor in Eq. (9) to facilitate comparison with Fourkas' results, but Eq. (9) can be simplified further by distributing  $D$ .

We can extend these results to light-sheet illumination created by scanning a laser. If we shine a narrow, collimated, laser beam onto a galvanometer in the aperture plane and scan the galvanometer, we create a weakly focused light sheet in the sample. If we scan the beam in the sample with a velocity much less than the beam waist radius divided by the coherence time, then the coherence of the laser is rendered ineffectual by the scanning—the light sheet is effectively composed of many incoherent beams. If we also ensure that the laser beam is weakly focused, we can ignore the excitation caused by the small fields aligned with the optical axis. Under slowly-scanned and weakly-focused light-sheet illumination, dipoles in the sample will be excited as if a single plane wave was incident. Therefore, we can find the absorption efficiency of a dipole in this case by taking the limit of Eq. (9) as  $\alpha \rightarrow 0$  [or by plugging Eqs. (1) and (2) into Eq. (7)] giving

$$\eta_{\text{abs}}^{\text{ray}} = \sin^2 \Theta \cos^2(\Phi - \phi_{\text{exc}}), \quad (11)$$

which is recognizable as Malus' law generalized to three dimensions. This means that light-sheet illumination is approximately equivalent to low-NA illumination with respect to the dipole orientations they excite. Notice that the absorption efficiency can take its maximum range of values ( $\eta_{\text{abs}} \in [0, 1]$ ) when  $\alpha = 0$ .

## 2.2. Detection Efficiency

In this section we will calculate the *detection efficiency*—the fraction of the power emitted by a single dipole that we detect. Fourkas calculated the detection efficiency when an ideal objective with its optical axis aligned with the  $\hat{\mathbf{z}}$  axis is focused on a single dipole and a polarizer is placed in the aperture plane [15]. He found that

$$\eta_{\text{det}}^{\text{pol}} = A + B \sin^2 \Theta + C \sin^2 \Theta \cos [2(\Phi - \phi_{\text{det}})], \quad (12)$$

where  $\phi_{\text{det}}$  is the angle between the transmission axis of the detection polarizer and the positive  $\hat{\mathbf{x}}$  axis.

To calculate the detection efficiency without a polarizer, we use Eq. (12) and take the sum of polarized detection efficiencies with orthogonal polarizer orientations to find

$$\eta_{\text{det}} = 2(A + B \sin^2 \Theta). \quad (13)$$

In this case the detection efficiency only depends on  $\Theta$ , not  $\Phi$ , because there is no detection polarizer. We have assumed that the absorption dipole moment is equal to the emission dipole moment.

Note that  $A$ ,  $B$ , and  $C$  in Eq. (10) are a factor of  $\frac{3}{2}$  larger than the expressions given by Fourkas. We found that Fourkas' expressions were incorrectly normalized (the limit of  $\eta_{\text{det}}$  as  $\alpha \rightarrow \frac{\pi}{2}$  should be  $\frac{1}{2}$ ), and the extra factor of  $\frac{3}{2}$  corrects the error. The extra factor of  $\frac{3}{2}$  is a constant multiplicative factor, so the correction is not angle-dependent which means that it does not affect Fourkas' orientation reconstruction. However, the correction does mean that Fourkas' algorithm underpredicts the total emitted intensity by a factor of  $\frac{3}{2}$ .

Also note that the detection efficiency can take its maximum range of values when  $B$  takes its maximum value, i.e. when  $\alpha = \arccos\left(\frac{1}{\sqrt{3}}\right) \approx 54.7^\circ$ . This means that the maximum modulation of detected intensities will occur when we choose a detection objective with  $\alpha \approx 54.7^\circ$ .

### 2.3. Oblique Illumination and Detection

In sections 2.1 and 2.2 we assumed that both the illumination and detection objectives had  $\hat{\mathbf{z}}$  aligned optical axes, i.e., we assumed traditional epi- or transmitted light illumination. To extend the forward model to oblique optical axes which allows for non-coincident illumination and detection objectives, we express the dipole orientation in a rotated coordinate frame using the following expressions

$$\Theta' = \arccos(\sin \psi \cos \Phi \sin \Theta + \cos \psi \cos \Theta) \quad (14)$$

$$\Phi' = \begin{cases} \arccos\left(\frac{\cos \psi \cos \Phi \sin \Theta - \sin \psi \cos \Theta}{\sqrt{1 - (\sin \psi \cos \Phi \sin \Theta + \cos \psi \cos \Theta)^2}}\right) & 0 \leq \Phi < \pi \\ -\arccos\left(\frac{\cos \psi \cos \Phi \sin \Theta - \sin \psi \cos \Theta}{\sqrt{1 - (\sin \psi \cos \Phi \sin \Theta + \cos \psi \cos \Theta)^2}}\right) & -\pi \leq \Phi < 0 \end{cases} \quad (15)$$

where  $\psi$  is the angle of a right handed rotation about the  $\hat{\mathbf{y}}$  axis that maps the  $\hat{\mathbf{z}}$  axis onto the new optical axis.

### 2.4. Intensity Measurements

The detected intensity is proportional to the product of the sample irradiance  $I_{\text{in}}$ , the absorption efficiency, and the detection efficiency

$$I \propto I_{\text{in}} \eta_{\text{abs}} \eta_{\text{det}}, \quad (16)$$

where the proportionality depends on the exposure time, the molecular quantum efficiencies, and other constant factors. Equation (16) is the forward model for a single intensity measurement. Figure 2 shows the efficiencies in three representative geometries. Note that in all cases there are multiple orientations that give the same intensity measurement. This means that a single intensity measurement does not give us enough information to reconstruct the orientation of a single dipole. Next, we will consider combining several intensity measurements to create polarized illumination microscopes that can reconstruct the orientation of single dipoles.

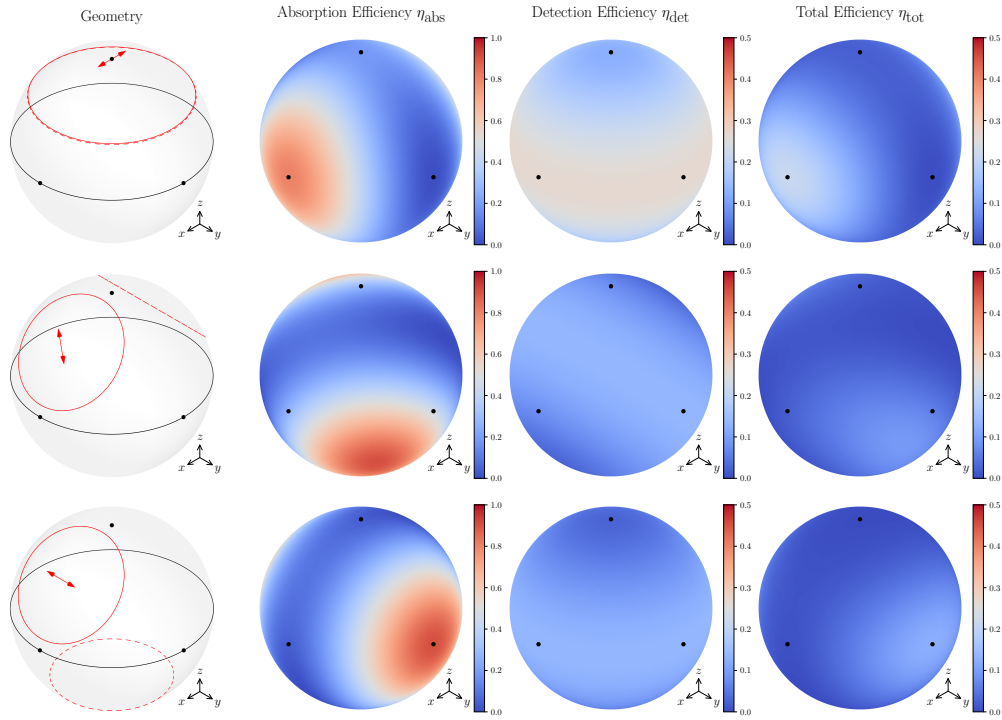


Fig. 2. Representative examples of single intensity measurements. Black dots indicate where the Cartesian unit vectors intersect the unit sphere.

**Columns left to right:** 1) schematics where the solid line encloses the illumination solid angle, the dashed line encloses the detection solid angle, and the arrow indicates the transmission axis of the illumination polarizer; 2) the absorption efficiency, see Eq. (9); 3) the detection efficiency, see Eq. (13); 4) the total efficiency, the product of the absorption and detection efficiencies.

**Rows top to bottom:** 1) coincident illumination ( $\text{NA} = 1.1$  with  $x$ -polarized light) and detection ( $\text{NA} = 1.1$ ); 2) non-coincident orthogonal illumination ( $\text{NA} = 0.8$ ) and detection ( $\text{NA} = 0.8$ ); 3) non-coincident  $135^\circ$ -separated illumination ( $\text{NA} = 0.8$ ) and detection ( $\text{NA} = 0.8$ ). All simulations use  $n = 1.33$ .

## 2.5. Polarized Illumination Microscope Configurations

One way to collect multiple intensity measurements is to add a universal compensator/polarizer to the illumination arm and rapidly select the incident polarization by changing  $\phi_{\text{exc}}$  [14]. All of the microscopes we will consider in this paper use four polarizations per illumination path with the polarization orientations separated by  $45^\circ$ .

We also consider several dual-view designs. We evaluate dual-view designs that allow for illumination and detection from both objectives (see [18] for a dual-view design). In all cases we consider the effect of varying the illumination and detection numerical aperture. We also consider asymmetric NA designs (see [21] for an asymmetric NA design) and the effect of asymmetric sample exposures. Note that we use the word *symmetry* to refer to dual-view designs with identical objectives and sample exposures and the word *asymmetry* to refer to dual-view designs with objectives that have a different NA or sample exposure.

All multiview microscopes are subject to steric constraints—the objectives must not collide with the cover slip or each other. We only consider microscope designs that meet these criteria.

### 2.6. Evaluation Metrics

Our goal is to evaluate the ability of a microscope design to estimate the orientation of a single dipole (via parameters  $\Theta$  and  $\Phi$ ) from intensity data. A common way to evaluate the ability to estimate the parameters  $\Theta$  and  $\Phi$  from the data is to calculate the Cramér-Rao lower bound (CRLB) for each parameter [22]. The CRLBs are given by the diagonal elements of the inverse of the Fisher information matrix, and they give the minimum variance of an unbiased estimator for each parameter. For each microscope design and dipole orientation we calculate the Fisher information matrix. We assume that the detected intensities are Poisson distributed, so the Fisher information matrix is given by

$$\mathbf{F} = \sum_{k=1}^N \frac{1}{I_k} \begin{bmatrix} \frac{\partial I_k}{\partial \Theta} \frac{\partial I_k}{\partial \Theta} & \frac{\partial I_k}{\partial \Theta} \frac{\partial I_k}{\partial \Phi} \\ \frac{\partial I_k}{\partial \Phi} \frac{\partial I_k}{\partial \Theta} & \frac{\partial I_k}{\partial \Phi} \frac{\partial I_k}{\partial \Phi} \end{bmatrix} \quad (17)$$

where  $I_k$  is the  $k$ th intensity measurement in a microscope that uses  $N$  intensity measurements. Agrawal et. al. used the square root of the product of the CRLBs multiplied by the Jacobian determinant,  $\sin \Theta \sqrt{\mathbf{F}_{0,0}^{-1} \mathbf{F}_{1,1}^{-1}}$ , to find the area of uncertainty in parameter space [11].

CRLBs and the associated area of uncertainty are parameterization dependent, i.e., if we choose a different coordinate system these metrics will change. We would like to compare microscope designs without choosing a parameterization, so instead we use

$$\sigma_\Omega \equiv \sin \Theta \sqrt{\det\{\mathbf{F}^{-1}\}} \quad (18)$$

as our evaluation metric. We calculate the determinant of the inverse Fisher information matrix—a parameterization-independent value called the *generalized variance* [23]—take the square root, then multiply by the Jacobian determinant,  $\sin \Theta$ . We call  $\sigma_\Omega$  the *solid-angle uncertainty* because it has units of steradians and is a parameterization independent measure of the orientation uncertainty.

For each microscope we calculate  $\sigma_\Omega$  at 10,000 approximately equally spaced points on the unit sphere. A desirable microscope design will have a small solid-angle uncertainty that is uniform for all dipole orientations. The most straightforward way to find the location and scale of the solid-angle uncertainty is to use the mean and variance, respectively. However, the solid-angle uncertainty can take extremely large values, e.g., when a fluorescent dipole is aligned with the optical axis of a single excitation objective. Such large values can change the mean and variance dramatically depending on the sample points, so we use the median and median absolute deviation (MAD)—the median of the data’s absolute difference from the median—as robust alternatives to the mean and variance.

To compare microscopes with different numbers of intensity measurements fairly, we kept the irradiance incident on the sample constant by choosing  $I_{\text{in}} = \frac{4000}{N}$ . Note that  $I_{\text{in}}$  is a measure of irradiance to the sample, not the detected intensity or the total intensity emitted by the molecule.

We also use the Fisher information matrix to calculate uncertainty ellipses for each microscope and dipole orientation. The general equation of an ellipse with axis radii  $a$  and  $b$  and rotation angle  $\gamma$  is

$$\frac{(x \cos \gamma + y \sin \gamma)^2}{a^2} + \frac{(x \sin \gamma - y \cos \gamma)^2}{b^2} = 1. \quad (19)$$

We calculate the ellipse parameters in terms of the Fisher information matrix using the following set of equations

$$\sigma_x = \sqrt{\mathbf{F}_{0,0}^{-1}} \quad (20)$$

$$\sigma_y = \sin \Theta \sqrt{\mathbf{F}_{1,1}^{-1}} \quad (21)$$

$$\sigma_{xy} = \sin \Theta \sqrt{\mathbf{F}_{1,0}^{-1}} \quad (22)$$

$$a^2 = \frac{\sigma_x^2 + \sigma_y^2}{2} + \sqrt{\frac{(\sigma_x^2 - \sigma_y^2)^2}{4} + \sigma_{xy}^2} \quad (23)$$

$$b^2 = \frac{\sigma_x^2 + \sigma_y^2}{2} - \sqrt{\frac{(\sigma_x^2 - \sigma_y^2)^2}{4} + \sigma_{xy}^2} \quad (24)$$

$$\gamma = \frac{1}{2} \arctan \left( \frac{2\sigma_{xy}}{\sigma_x^2 - \sigma_y^2} \right). \quad (25)$$

Equations (20)–(25) are identical to those found in [24] with an additional factor of  $\sin \Theta$  on Eqs. (21) and (22) to account for the non-Euclidean geometry of the sphere. Instead of plotting ellipses with widely varying radii on the same figure, we chose a constant major axis radius. This means that the uncertainty ellipses indicate the relative size of uncertainty in different directions, not the absolute size of the uncertainty.

The solid-angle uncertainty and the uncertainty ellipse are good local measures of orientation uncertainty, but they are insensitive to degeneracies with distant dipole orientations. For example, all of the intensity measurements in this paper are identical under inversion of the dipole orientation [ $I(\Theta, \Phi) = I(\Theta + \pi, \Phi)$  in Eqs. (9), (13), and (16)], but the solid-angle uncertainty and the uncertainty ellipse give no indication of this degeneracy. For this reason we also use the number of degeneracies as a measure of a microscope's ability to estimate the orientation of a dipole from intensity measurements. A small number of degeneracies is important for a microscope to find the orientation of a dipole—a twofold degenerate microscope can find the orientation of a dipole down to the hemisphere while a fourfold degenerate microscope can only find the orientation down to the quadrant.

To calculate and display these evaluation metrics we use NumPy [25] for numerical computation, SymPy [26] for symbolic computation, Matplotlib [27] for high-level plotting, VisPy [28] for 3D rendered plots, and Asymptote [29] for 3D line plots.

### 3. Results

Figure 3 shows our results for single-view designs where a single objective is used for illumination and detection. We swept through the illumination and detection NA while keeping the sample irradiance constant, and we found that the lowest median and MAD of the solid-angle uncertainty occurs with a small illumination NA and a large detection NA where  $\alpha \approx 65^\circ$  [see Fig. 3(e) at  $NA_{\text{det}} \approx 1.2$ ]. A small illumination NA maximizes the range of absorption efficiencies, while a large detection NA optimizes the number of detected photons and the range of the detection efficiencies. The optimal detection NA is slightly larger than  $\alpha = 57.4^\circ$  because increasing the detection NA reduces the effect of shot noise. Note the relative importance of illumination and detection NAs—reducing the illumination NA (an inexpensive modification requiring underfilling the aperture plane) improves the solid-angle uncertainty much less than increasing the detection NA (an expensive modification requiring a higher-NA objective). Also note in Fig. 3(c) that single-view designs suffer from high orientation uncertainty when the dipoles are oriented along the optical axis (the dipoles are not efficiently excited or detected), near the transverse plane (it

is ambiguous whether the dipole is oriented above or below the transverse plane, see Fig. 3(b), and near the polarizer orientations [it is ambiguous whether the dipole is on either side of the polarizer orientation, see Fig. 3(b)].

The single-view microscope in Fig. 3 is fourfold degenerate [ $I(\Theta, \Phi) = I(\Theta + \pi, \Phi) = I(\Theta, \Phi + \pi) = I(\Theta + \pi, \Phi + \pi)$ ] in Eqs. (9), (13), and (16)]. The first twofold degeneracy is due to the usual inversion degeneracy—the dipole is an axis rather than a direction. A second twofold degeneracy is present in single-view designs—the microscope cannot distinguish between dipoles reflected through the transverse plane. Evidence of the second degeneracy is found in Figs. 3(b) and 3(c) which show the ambiguity of whether the dipole is oriented above or below the transverse plane. Near the transverse plane this ambiguity is evident in the high solid-angle uncertainty, but far from the transverse plane evidence of the ambiguity is lost. Adding a second view and taking eight intensity measurements instead of four removes this degeneracy [see Eqs. (14) and (15)], so the dual-view microscopes we consider in this paper are only twofold degenerate. This means that while dual-view microscopes can find the orientation of a dipole up to the hemisphere, single-view microscopes can only find the orientation of a dipole up to the quadrant.

Figures 4 and 5 show our results for dual-view symmetric designs. We illuminate from one objective and detect from the other for four polarization orientations, then we repeat the polarization orientations with the same objectives in reversed roles. In Fig. 4 we sweep through the NA of both objectives and the angle between the objectives while considering steric constraints. Note how adding a second view removes the high uncertainty region in the transverse plane. The dual-view microscope still has high uncertainty regions near the optical axes, but the uncertainty is reduced by almost two orders of magnitude compared to the single-view microscope. We find that the lowest median of the solid-angle uncertainty occurs with the largest possible NA objectives. We also find that increasing NA always lowers the MAD, but orthogonal arms are not always optimal. At large NA, it is advantageous to move the objectives together or against the cover slip. Given the high uncertainty in the transverse plane for a single-view shown in Fig. 3(c), we can see why oblique views perform better than orthogonal views—oblique views are complementary because the regions of high orientation uncertainty from each view do not overlap.

Figure 5 shows our results when we used a dual-view symmetric orthogonal design and varied the illumination and detection NA. Our results are similar to the single-view case in Fig. 3. We find that optimal designs use a small illumination NA and a large detection NA. As we discussed in Section 2.1, low-NA illumination is approximately equivalent to light-sheet illumination for the task of estimating the orientation of dipoles. Therefore, the preference for low-NA illumination also implies that dual-view light-sheet illumination geometries are an excellent choice for uniformly reconstructing the orientation of single dipoles.

Figure 6 shows our results for dual-view asymmetric light-sheet illumination designs. We used light-sheet illumination on both sides and kept the objectives orthogonal so that the light sheet from one objective illuminates the focal plane of the other objective. Then, we swept through the NA of one objective while maximizing the NA of the other objective so that both objectives would touch the cover slip and each other [ $\alpha_1 + \alpha_2 = 90^\circ$  in Fig. 6(a)]. We swept through the NA asymmetry and the sample-exposure asymmetry while keeping the sample irradiance constant, and found that symmetric designs are at a local minimum of the median and MAD of the solid-angle uncertainty. We also found that at extreme asymmetries where the exposure from the low-NA arm is much larger than the exposure from the high-NA arm [top-left and bottom-right corners of Figs. 6(d) and 6(e)] the median and MAD are comparable to the symmetric light-sheet microscope. This means that if a very high-NA objective is available and a low-NA objective can provide light sheet illumination, this microscope will perform comparably with a dual-view microscope with two medium-NA objectives. Note that this asymmetric exposure configuration maximizes the use of the high-NA detection objective—if a high-NA objective is available

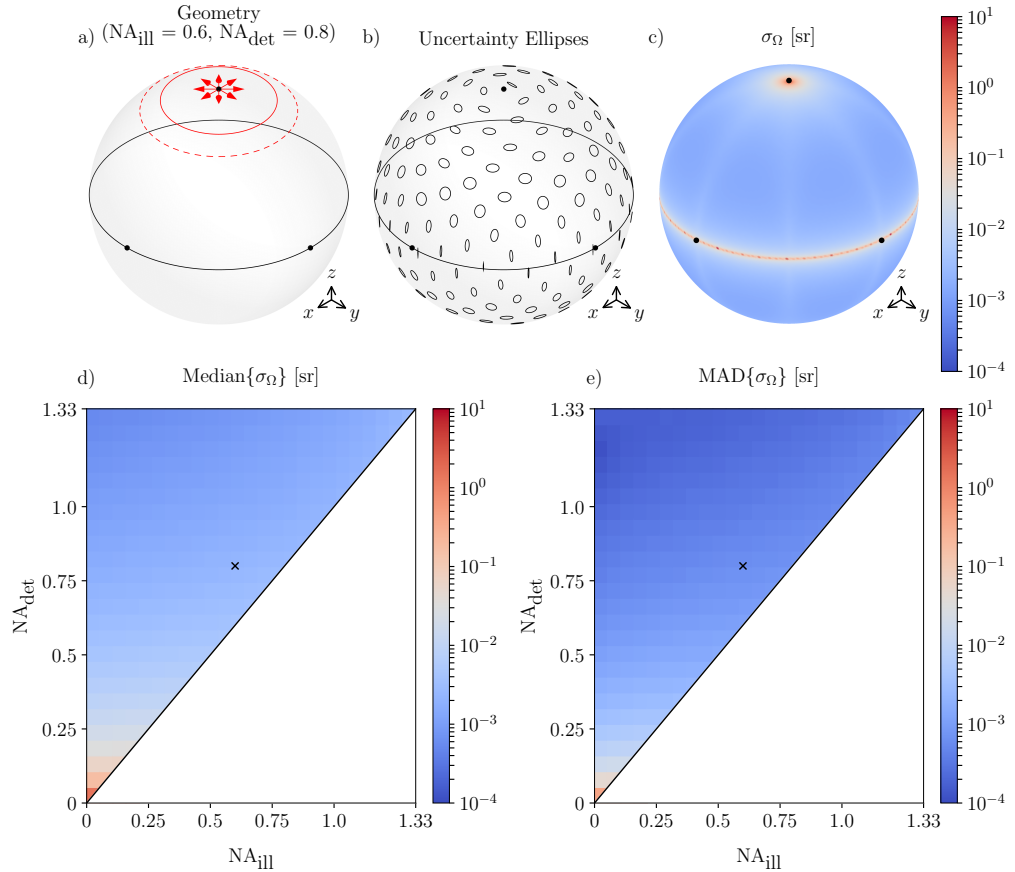


Fig. 3. Single-view microscope with varying illumination and detection NA. a) Schematic of a single-view four-polarization epi-illumination microscope. The red arrows indicate the four illumination polarization orientations—one for each intensity measurement. b) Uncertainty ellipses for the microscope in a). The ellipses indicate the relative size of the uncertainty in different directions, not the absolute size of the uncertainty. c) Solid-angle uncertainty for the microscope in a). The solid-angle uncertainty is a measure of the absolute size of the uncertainty in all directions. d) Median of the solid-angle uncertainty as a function of illumination and detection NA. e) MAD of the solid-angle uncertainty as a function of illumination and detection NA. The microscope configuration in a), b), and c) is indicated by a cross in d) and e).

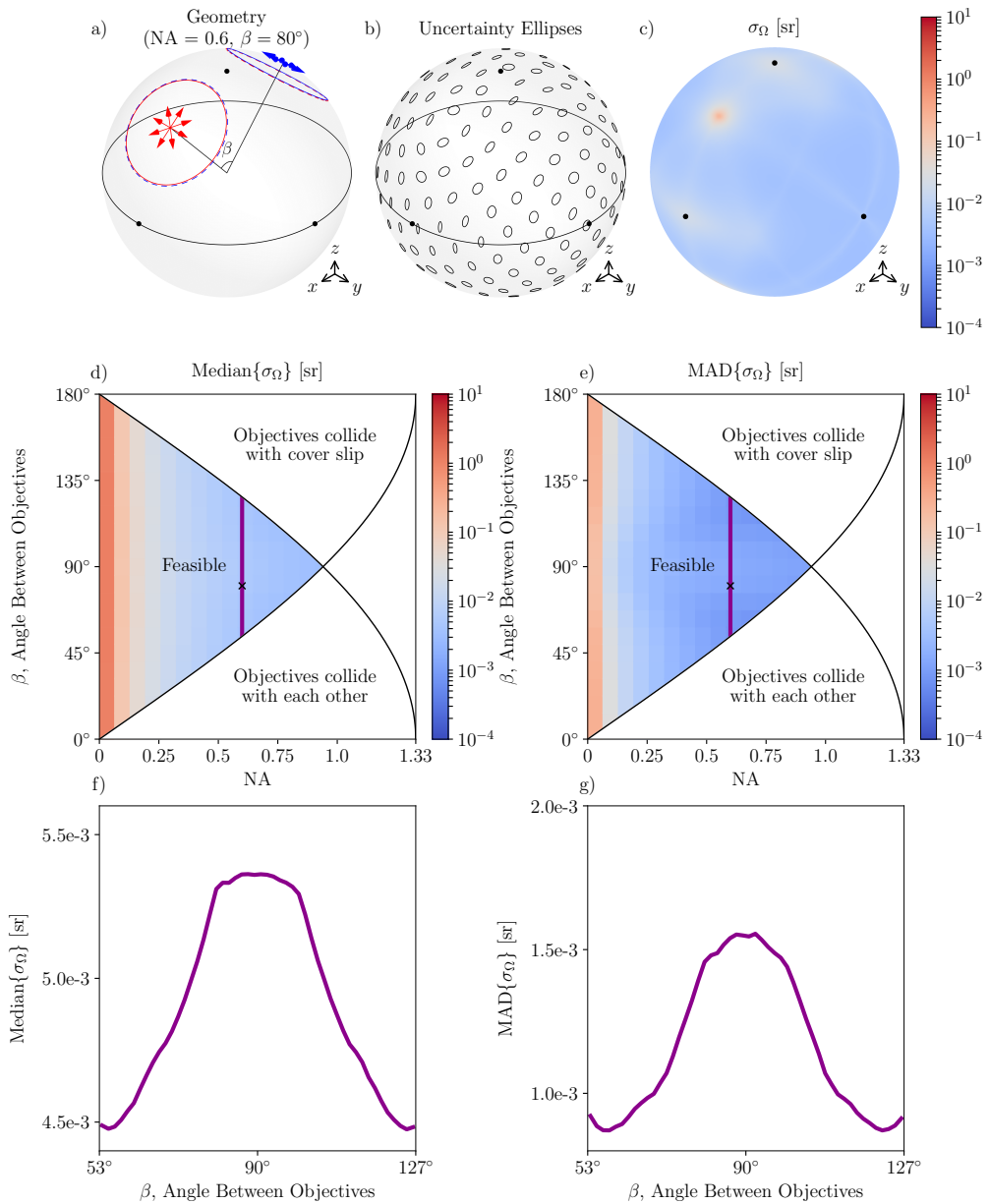


Fig. 4. Dual-view symmetric designs with varying NA and angle between objectives. a) Schematic of the microscope. We illuminate with the first objective (red solid) and detect from the second objective (red dashed). Then we illuminate from the second objective (blue solid) and detect from the first objective (blue dashed). b) Uncertainty ellipses for the microscope in a). The ellipses indicate the relative size of the uncertainty in different directions, not the absolute size of the uncertainty. c) Solid-angle uncertainty for the microscope in a). The solid-angle uncertainty is a measure of the absolute size of the uncertainty in all directions. d) Median of the solid-angle uncertainty as a function of NA and the angle between the objectives. e) MAD of the solid-angle uncertainty as a function of NA and the angle between the objectives. The microscope configuration in a), b), and c) is indicated by a cross in d) and e). f) Median of the solid-angle uncertainty as a function of the angle between the objectives when NA=0.6. g) MAD of the solid-angle uncertainty as a function of the angle between the objectives when NA=0.6. The profile in f) and g) is taken along the purple line in d) and e).

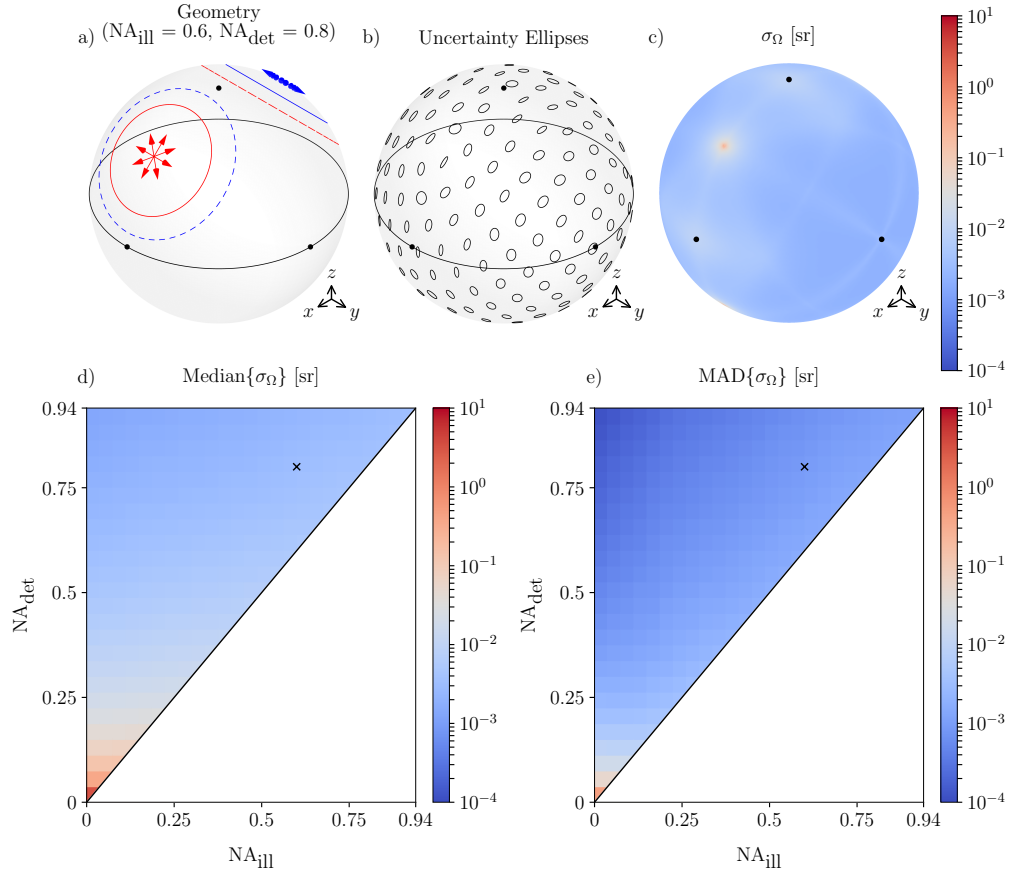


Fig. 5. Dual-view symmetric orthogonal designs with varying illumination and detection NA. a) Schematic of the microscope. b) Uncertainty ellipses for the microscope in a). The ellipses indicate the relative size of the uncertainty in different directions, not the absolute size of the uncertainty. c) Solid-angle uncertainty for the microscope in a). The solid-angle uncertainty is a measure of the absolute size of the uncertainty in all directions. d) Median of the solid-angle uncertainty as a function of illumination and detection NA. e) MAD of the solid-angle uncertainty as a function of illumination and detection NA. The microscope configuration in a), b), and c) is indicated by a cross in d) and e).

it should be used for detection as much as possible. Figure 6 also shows that designs with slightly asymmetric NA can trade off a low solid-angle uncertainty median for a low solid-angle uncertainty MAD by changing the sample exposure ratio.

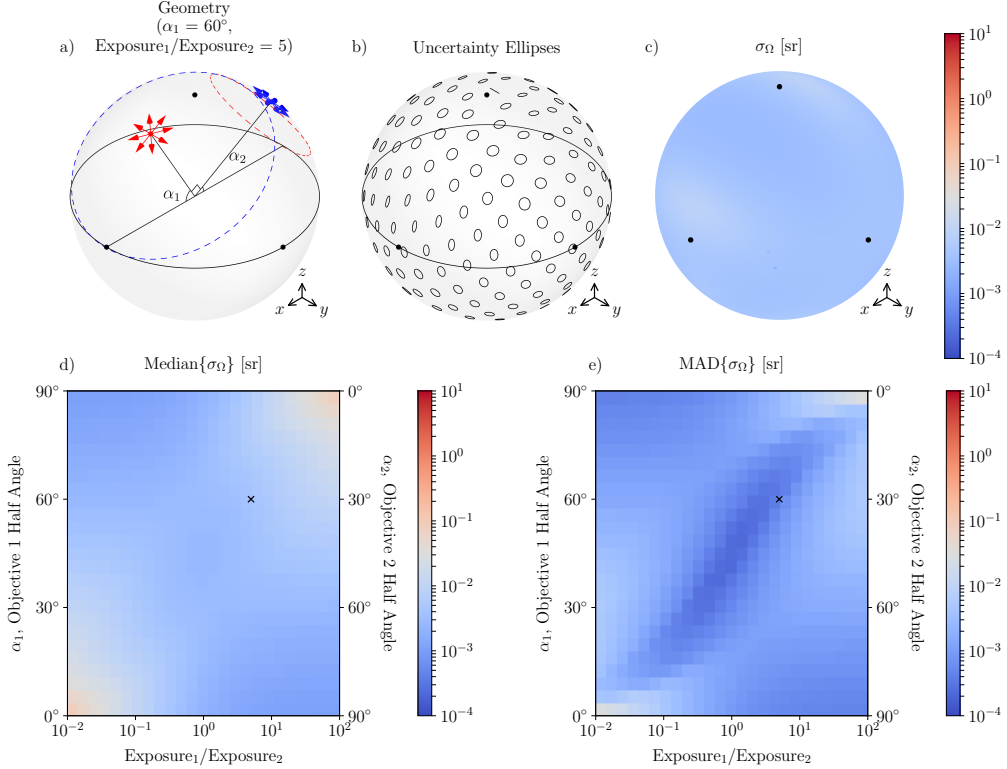


Fig. 6. Dual-view asymmetric light-sheet illumination designs with varying NA and sample exposure asymmetry. a) Schematic of the microscope. b) Uncertainty ellipses for the microscope in a). The ellipses indicate the relative size of the uncertainty in different directions, not the absolute size of the uncertainty. c) Solid-angle uncertainty for the microscope in a). The solid-angle uncertainty is a measure of the absolute size of the uncertainty in all directions. d) Median of the solid-angle uncertainty as a function of NA and sample exposure asymmetry. e) MAD of the solid-angle uncertainty as a function of NA and sample exposure asymmetry. The microscope configuration in a), b), and c) is indicated by a cross in d) and e).

Table 1 shows a summary of our evaluation metrics for microscopes in each class. The single-view microscope with a small illumination NA and high detection NA has the lowest solid-angle uncertainty median but the largest max and fourfold degeneracy. The dual-view oblique symmetric microscope with an intermediate NA performs reasonably well on all three metrics, while the dual-view orthogonal symmetric light-sheet microscopes with large NA perform very well on all three metrics.

#### 4. Discussion and Conclusions

In this work we have developed a model to predict the intensities measured by polarized illumination microscopes in a wide range of geometries, developed metrics to measure the ability of a microscope design to estimate the orientation of single dipoles, and used these metrics to

Table 1. Comparison of designs in each class of microscope. All solid-angle uncertainty statistics are in steradians.

Microscope Type	$n$ -fold Degeneracy	$\text{Max}\{\sigma_\Omega\}$	$\text{Median}\{\sigma_\Omega\}$	$\text{MAD}\{\sigma_\Omega\}$
Single-view ( $\text{NA}_{\text{ill}}=0$ , $\text{NA}_{\text{det}}=1.1$ )	4	$3.04 \times 10^0$	$8.20 \times 10^{-4}$	$1.48 \times 10^{-4}$
Dual-view oblique symmetric ( $\text{NA}=0.6$ , $\beta=53^\circ$ )	2	$1.35 \times 10^{-1}$	$4.49 \times 10^{-3}$	$9.17 \times 10^{-4}$
Dual-view orthogonal symmetric light-sheet ( $\text{NA}=0.8$ )	2	$6.23 \times 10^{-3}$	$1.79 \times 10^{-3}$	$1.65 \times 10^{-4}$
Dual-view orthogonal symmetric light-sheet ( $\text{NA}=0.94$ )	2	$3.13 \times 10^{-3}$	$1.28 \times 10^{-3}$	$1.14 \times 10^{-4}$

compare a wide range of microscope designs. Our main result is a short list of design heuristics that can be used to design polarized-illumination single-dipole orientation microscopes:

- Single-view microscopes benefit from a small illumination NA and a large detection NA with  $\alpha \approx 65^\circ$ .
- Dual-view microscopes outperform single-view microscopes along several metrics. Dual-view microscopes have fewer degeneracies, lower median and MAD solid-angle uncertainty, and no high solid-angle uncertainty region in the transverse plane.
- High-NA dual-view microscopes are optimal when the two views are oblique. Oblique views are complementary because their high uncertainty transverse planes do not overlap.
- Symmetric NA dual-view orthogonal light-sheet microscopes provide a good compromise between cost, solid-angle uncertainty median, and solid-angle uncertainty MAD. Asymmetric NA dual-view orthogonal light-sheet microscopes can improve the solid-angle uncertainty median or MAD by changing the sample exposure ratio between the two views.

Our results are limited in several ways. First, we only consider single molecules in homogeneous environments whose absorption and emission dipoles are parallel. We ignore light reflected from the cover slip and any other inhomogeneities in the sample. If we considered light reflected from the cover slip we expect that the results would put a lower weighting on large detection NAs because we would collect more light. Second, we only considered ideal, aplanatic, polarization-preserving objectives. In practice, these conditions are not always satisfied. For example, the power from high-NA rays is usually apodized by a factor of  $\frac{n}{\cos\Theta}$  [30]. Therefore, our results are most accurate for paraxial rays and get progressively worse for non-paraxial rays, although our major conclusions would not change if we included this apodization factor. The main advantage of ignoring apodization is the tractability of the problem—we have provided approximate closed-form solutions for the illumination and detection efficiencies that have allowed us to draw useful design conclusions. Third, we have used a Poisson noise model which ignores noise introduced by the detector. Detector noise can be a large fraction of the total noise at low intensities, so including detector noise would increase the informational value of high intensity measurements. Therefore, we expect that including the effects of detector noise would favor microscopes with a large detection NA. Finally, we have focused on the task of estimating the orientation of dipoles and ignored the equally important task of estimating their location. The task of jointly estimating the orientation and location of single dipoles from multiple views is a topic for future work.

To compare the microscopes in this paper we used a fixed irradiance incident on the sample. We think that this is the fairest way to compare microscopes with different numbers of intensity measurements. However, in cases where sample irradiance and time are not an issue it may be more useful to compare microscopes with the same total detection irradiance per measurement. This comparison would favor microscopes with many intensity measurements even more than the results in this paper because equal detection irradiance would improve photon counting statistics.

We have considered single- and dual-view microscopes in a variety of cases, but other multiview microscopes can be analyzed with the framework we have developed. Wu et. al. have developed a three-view design with a third objective below the cover slip [20]. Light-field detection schemes are also a type of multiview microscope [31], and we plan to extend our analysis to this case in future work.

The models in this paper only consider estimating the orientation of fixed dipoles, but real dipoles change their orientation during measurement. Therefore, it is necessary to comment on the applicability of our results to dynamic dipoles. In general, using the models in this paper to estimate the orientation of rotating dipoles will lead to incorrect results. However, if a dipole rotates through a small solid angle during the measurement, the models in this paper will give a slightly biased estimate of the average orientation of the dipole. The direction and size of the bias has not been characterized in detail. In future work we will model dynamic dipoles and attempt to estimate the average dipole orientation and the dipole's orientation distribution. Single-view polarized illumination techniques have already been used to study the orientation distribution of ensembles of dynamic dipoles [3, 4], but multiview polarized illumination microscopes have not been investigated for this purpose.

We have only considered polarized illumination. In the introduction we discussed why we prefer polarized illumination to polarized detection, but there is information to be gained by adding polarized detection to the techniques discussed in this paper. Adding a polarization splitter to the detection arm can increase the information available for reconstructing the orientation of a single dipole without increasing the acquisition time.

We conclude that multiview microscopes are useful tools for determining the orientation of single dipoles. Using simple design heuristics, we can design polarized illumination multiview microscopes that can determine the orientation of single dipoles with a small and uniform orientation uncertainty.

## Funding

National Institute of Health (NIH) (R01GM114274, R01EB017293).

## Acknowledgments

TC was supported by a University of Chicago Biological Sciences Division Graduate Fellowship. HS and PL were supported by Marine Biological Laboratory Whitman Center Fellowships. HS was supported by the Intramural Research Programs of the National Institute of Biomedical Imaging and Bioengineering.

## Disclosures

The authors declare that there are no conflicts of interest related to this article.